Illuminating the physics of melting during laser-based manufacturing of IN718 by measuring laser light reflections

David Deisenroth[1], Haoran Shi[2], Moritz Wittemer[3], Nismath Valiyakath Vadakkan Habeeb[4], Kevin Chou[4], Wenda Tan[2], Jordan Weaver[1], and Katrin Wudy[3]

[1] National Institute of Standards and Technology
100 Bureau Dr., Gaithersburg, Maryland 20899, USA
e-mail: david.deisenroth@nist.gov

[2] University of Michigan
2424 GGB, 2350 Hayward, Ann Arbor, MI 48109, USA

[3] Technical University of Munich
Professorship of Laser-Based Additive Manufacturing
Freisinger Landstrasse 52, 85748 Garching bei Muenchen, Germany

[4] University of Louisville
132 Eastern Pkwy., Louisville, Kentucky 40292, USA

Abstract

It has been known since the early years of laser welding that measuring of the energy absorbed into, and reflected away from, metallic materials can provide valuable insights into the physics of the melting process. This work uses a recently developed high-fidelity measurement of the directional distribution of reflected laser light, an integrating hemisphere to measure total reflected laser power, as well as cross sections of the melt tracks perpendicular and parallel to the scan direction. Arrays of five tracks with offset antiparallel scans are melted in bare plate nickel superalloy 718 at processing parameters of relevance to laser-based powder bed fusion of metals (PBF-LB/M). All processing parameters are held constant, except power is varied from 50 W to 545 W. The instantaneous laser coupling (laser absorption) and melt depth along the track increase or decrease nearly in unison within the desirable range of applied power. The strong correlation weakens in the high power, deep keyholing mode when absorption saturates. The directional distributions of reflected laser light show distinct patterns and features that correspond to the stages of the melting process and to the state of the vapor depression. A hazy reflection distribution forms when the incident laser reflects from a ground metal surface, a circular pattern with concentric rings forms in conduction mode, and then radial streaks form in keyhole mode. A high-fidelity melt pool model that includes ray tracing shows favorable agreement between the experimental and simulated reflections at 185 W, 285 W, and 485 W during steady-state melting. The model was used to determine that the physical origin of prominent streaking features of the reflection distributions originate from a single reflection from surface ripples at the cusp of the melt pool. This study establishes reflected laser light measurements as a high-fidelity diagnostic and model validation tool to inform process monitoring approaches in industrial PBF-LB/M systems.

Keywords

Laser-based metal additive manufacturing, laser-based powder bed fusion of metals, laser absorption, laser coupling, distribution of reflected laser light, process monitoring, model validation

Introduction

The physics of melting metallic materials with lasers has been a topic of interest for more than a half century [1]. It has been long established that with increasing applied volumetric energy density (VED $\propto$ $P/v/D^2$, where P is the laser power, v is the scan speed, and D is the laser beam diameter), several modes of heating and melting occur. It has further been established that each one of these melting modes strongly relates to the energy absorptivity into, and reflection away from, the material.

At the lowest VEDs, the solid metal surface is heated without melting and the absorptivity takes on the intrinsic value of the material that is typically measured on a sample with an abrasive ground surface [2]. The expected absorptivity value of roughened, solid, nickel superalloy 718 (IN718) is expected to be approximately 0.38. This estimate is based on measurements of nickel superalloy 625 (IN625), which has very similar physical properties to IN718, observed in calorimetric non-melting tests in previous work [3]. Furthermore, this value agrees well with the measured emissivity (equivalent to absorptivity at thermodynamic equilibrium) of high-purity Ni (the majority constituent of a nickel superalloy) near the solidus temperature of IN718 (1278 °C) at 1070 nm [4].

As VED increases, the solid surface changes phase into liquid and the absorptivity typically decreases to that of the given metal as a liquid. It is expected that the laser energy that is not absorbed is reflected in a single specular reflection. A further increase in VED causes the liquid to begin evaporating, and the recoil pressure from evaporation causes a depression to form in the liquid surface. This "vapor depression" allows for multiple laser light reflections onto the material, which increases the total laser energy absorption [5]. This absorption is no longer an intrinsic material property but rather an effective absorption that depends on the total amount of light trapped by multiple reflections. As the VED is further increased, the vapor depression deepens and becomes a "keyhole" that can be much deeper than it is wide, and the process can approach near total absorptivity of the laser energy.

The absorptivity can be directly measured through calorimetry, which has historically been done for laser welding [5] and more recently for laser-based powder bed fusion of metals (PBF-LB/M) [3,6]. Absorptivity measurements have shown to be a useful validation tool for complex melt pool scale models that include ray tracing [6]. However, even though calorimetry is a direct measurement of laser energy absorptivity into the melting process, this measurement method does not provide any information about the spatial or temporal process dynamics.

Fabbro et al. [2] implemented an integrating sphere to temporally measure the total reflected laser power from the welding process. The photodiode had a temporal resolution of approximately 10 kHz, and the dynamics of the reflected power were measured at several levels of incident laser intensity, which provided novel insights into keyhole formation and melting physics. Wittemer and Wudy [7] used the integrating sphere approach applied to PBF-LB/M research, providing clear evidence of the formation of a vapor depression with increasing VED [7]. Lane et al. [8] showed relationships between inline melt pool emission signals, melt track surface features, and reflected laser power. Furthermore, the temporal dynamics from integrating sphere data have provided correlation with the formation of keyhole porosity with oscillation frequencies on the order of 25 kHz [9]. These reflected laser light measurements further corroborated the high-fidelity melt pool dynamics predicted by the computational model.

Mehmetli et al. [10] positioned a pyroelectric detector at dozens of equidistant positions around the melt pool and repeated a specific laser welding experiment at each detector position, effectively mapping out the hemispherical distribution of reflected laser light. Although the hemispherical distribution of reflected laser light was reported, this approach was essentially developed as an alternative to enshrouding the process with an integrating sphere. Wittemer et al. [11] employed a related approach for PBF-LB/M process monitoring, in which four parabolic dish collectors were positioned on the ceiling of the process chamber to detect the reflected laser light. This monitoring setup was used to capture reflected laser light in a real process environment where spherical and hemispherical enclosures would limit the laser working area and interfere with the feedstock delivery process in PBF-LB/M. It was found that the threshold for vapor depression formation can be detected by a characteristic change in the direction of reflection.

Directionally resolved reflection measurements have shown utility for validating high-fidelity computational models in recent work, with qualitative agreement between the reflection patterns and resulting melt depth [12]. This demonstrated that despite any physical assumptions or approximations, the melt pool scale model could quite reasonably predict physical outcomes of the melting process. Such melt pool scale models are part of the larger framework of models under development that can be used for prediction of material structure and performance based on processing conditions, with the greater goal of qualification and certification of additively manufactured metal components for critical applications [13,14].

This work uses a recently developed high-fidelity measurement of the directional distribution of reflected laser light [12], an integrating hemisphere to measure the total reflected laser power [3], as well as cross sections of the melt tracks perpendicular (widthwise) and parallel (lengthwise) to the scan direction of a five-track melt pad with processing parameters of relevance to PBF-LB/M [15]. Because these reflection distribution measurements have reached new levels of fidelity, our goal was to 1) test if the model could predict prominent reflection features (b) if the model could help interpret the experimentally measured reflection features.

Relationships between total reflected light and melting characteristics have been demonstrated across a wide variety of process conditions and alloys [5,6,9,10,16]. This novel method for directionally resolved measurement of laser light patterns has to date only been studied for nickel alloys and a limited number of process conditions; however, we expect that the reflection patterns related to the surface geometry and process modes will generalize. The intensity of the reflection and process conditions at which these patterns occur will be material dependent.

Nomenclature

In this work, “dynamic coupling” is the portion of applied laser power that is not reflected from the melting process. The dynamic coupling (α_{LC}) value is determined by measuring the reflected laser power (P_ρ), dividing that value by the applied laser power (P), and subtracting it from unity (making the value unitless, with a range from 0 to 1), i.e., $\alpha_{LC} = 1 – P_\rho / P$. The “energy coupling” is the time average of the dynamic coupling along the total length of a melt track. “Laser coupling” can refer to either the dynamic coupling or energy coupling, when distinguishing between the two is not necessary. Laser coupling is an approximation of laser absorption into the melting process, but it is not directly referred to as such, because it is an indirect measurement of absorptivity. Other power transfer mechanisms may occur during the melting process, such as power transfer to the latent heat of vaporization and/or laser power absorption into the plume of process byproducts [17].

“Conduction mode” melting refers to a condition when the “vapor depression” is relatively shallow. As the vapor depression grows significantly deeper, the melting mode transitions to “keyholing.” The aspect ratio of 2× the depth divided by the width provides some indication of the melting mode because the vapor depression and melt pool depth are tightly linked. In this work, we associate conduction mode with an aspect ratio < 1.

"Hazy reflection distribution" refers to a hemispherical reflection distribution that has components that are both diffuse and specular. In this work, hazy reflection distributions subtend a solid angle of less than 45° from normal and are characteristic of a ground metal surface.

Experimental methods

The experiments in this study are performed on the Fundamentals of Laser-Matter Interaction (FLaMI) testbed at the National Institute of Standards and Technology (NIST). The FLaMI system is a very accurate, well-characterized, and highly configurable laser processing testbed [18]. Two sets of melting experiments are performed on the FLaMI system with comparable melting conditions between the two sets, but the differing laser reflection metrology required slight differences in melting conditions. The experimental parameters are designed to partially replicate those of the 2025 Additive Manufacturing Benchmark Series AMB2025-07 Challenge Problems [19], with the addition of laser reflection metrologies and at multiple laser powers; antiparallel scan tracks are a common scan pattern used for PBF-LB.

Sample preparation

Sample substrates are cut from a rolled and annealed IN718 sheet. The material certificate for the as-received IN718 sheet is available in the AMB2025-07 Challenge Problem Calibration Data [19]. The sheet was 3.17 mm (1/8 in) thick and was cut to produce 25.4 mm × 25.4 mm (1 in × 1 in) bare plate samples. The bare plates are then random-orientation ground with 120 grit SiC paper. The resulting surface roughness was measured to be Sa = 0.3 μm ± 0.1 μm by focus variation.

Laser processing conditions

Arrays of five tracks with offset antiparallel scans were melted into the bare plates, as shown in Fig. 1. The center of the laser beam was scanned with an assumed offset of 0.08 mm. It is common to use a beam offset to ensure the melt tracks fit inside the desired geometry. In this case, the beam offset was optimized for a laser power of 285 W, the nominal pad geometry was 5 mm × 0.6 mm, and the distance of each track with the laser on was 4.84 mm. This scan strategy was fixed for all experiments because the intention was to vary only one parameter, which was laser power. As expected, this resulted in a pad geometry that was slightly smaller with lower laser powers and slightly larger with higher laser powers.

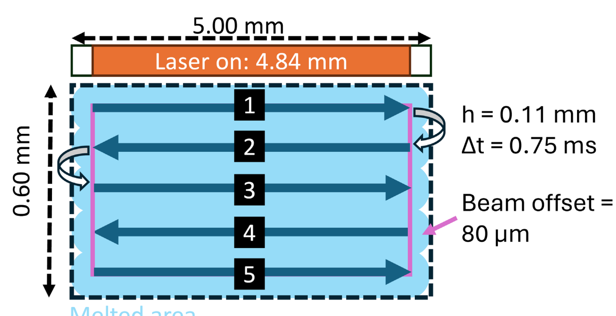

Fig. 1. Illustration of laser scan strategy for 5 mm × 0.6 mm pad with a 0.75 ms laser turnaround time. (FIGURE WIDTH: 1 COLUMN)

The processing conditions are slightly different in the laser coupling experiments and the directionally resolved reflected laser light experiments. The shared conditions for both sets of experiments are summarized in Table 1. The uncertainties of the laser processing conditions are described in detail in Deisenroth et al. [18]. The ranges in pressure, temperature, and roughness indicated in Table 1 are the maximum variation across all sets of experiments in this work.

Table 1: Base laser processing conditions

Laser spot size (Gaussian)	72 µm
Laser energy distribution	Circular Gaussian
Laser wavelength	1070 nm
Scan speed	960 mm/s
Track length (nominal)	5 mm
Hatch spacing	110 µm
Turnaround time	0.75 ms
Inert gas	Argon
Oxygen level	< 600 ppm
Chamber pressure	(101 ± 2) kPa
Substrate and chamber temperature	(23 ± 1) °C
Surface roughness (Sa)	(0.3 ± 0.1) µm

The differences in the processing conditions from the laser coupling experiments to the directionally resolved reflected laser experiments will be described in the following subsection.

Laser coupling

The laser coupling experiments are performed with a wider range of power levels, and then a down-selected set of powers was used for the directionally resolved experiments. The laser processing conditions that differ from the directionally resolved experiments are summarized in Table 2. The scan and hatch directions are orthogonal, the beam incidence angle is approximately 6° off-normal, and the gas flow conditions are different between the two sets of experiments. These variations are expected to minimally affect process outcomes, particularly melt depth. The differences in processing conditions are necessitated by the differences in the experimental metrology between the laser coupling and directional resolved measurements.

Table 2: Processing conditions unique to the laser coupling experiments

Laser power	50 W to 545 W
Scan direction	±y
Hatch direction	-x
Gas flow speed (z = 3 mm)	3.7 m/s
Gas flow direction	+x
Laser incidence angle	(6 ± 0.5)°

An integrating hemisphere was used to measure the total reflected laser light, which is described in detail in Deisenroth et al. [3]. In summary, the photodetector signal from within the integrating hemisphere is calibrated against a known applied power and reference mirror. Thus, the total reflected laser power can be measured despite its directional distribution (i.e., fully integrated result).

It must be noted, though, that light can be reflected out of the laser port or lost at high angles, and the amount of unmeasured power may depend on the directional distribution of the reflection. In this experiment, port losses are mitigated by applying the laser at an incidence angle of approximately 6° off-normal in the -x direction, as illustrated in Fig. 2. The laser is then scanned in the ±y direction with hatching in the -x direction to further minimize the loss of specular reflection components out of the laser inlet port. The results of perpendicular cross sections of the melt tracks show that this angle does also slightly angle the melting profile in the material, but this subtle effect is not expected to significantly change the laser coupling.

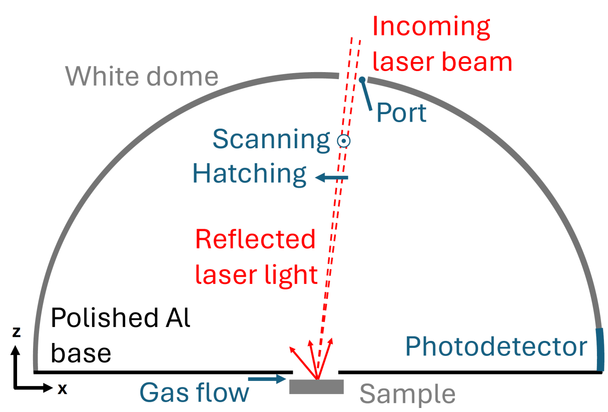

Fig. 2. Illustration of laser coupling experimental setup. (FIGURE WIDTH: 1 COLUMN)

Laser coupling uncertainty

As described in previous work, the relative standard uncertainty (Type B, k = 1) of the reflected laser power is 3.5 % [3]. Using the typical values of reflected power at several laser power steps, the measurement uncertainty is translated into relative uncertainty of the laser coupling, as shown in Table 3. It should be noted that laser coupling is an indirect measurement of absorptivity that does not account for other power transmission mechanisms such as evaporation or laser absorption into the plume of process byproducts.

Table 3: Relative standard uncertainty of laser coupling at several laser powers

Laser power (W)	Typical reflected power (W)	Typical energy coupling uncertainty (%)
50	35	7.8
113	68	5.5
135	69	3.7
185	73	2.3
285	75	1.2
385	73	0.8
485	97	0.8

545	86	0.7

In this work laser coupling was sampled at 1 MHz and then smoothed with 50-point moving average, effectively resolving the data at 20 kHz. This allows for clearer trend visualization with reduced high-frequency fluctuations. Frequencies at greater than 20 kHz can be associated with keyhole pore formation [9], but such defects are not observed in this work. Nevertheless, use of high-frequency fluctuations may be the subject of future model validation work, and the 1 MHz resolution data will be available in the National Institute of Standards and Technology (NIST) Public Data Repository [20].

Reflected laser light distributions

As mentioned previously, the directionally resolved reflected laser experiments are performed at fewer power levels than the laser coupling experiments. Also, the scan and hatch directions are orthogonal to those of the laser coupling experiments, as shown in Table 4. The gas flow direction was downward onto the sample, instead of horizontally across, with a nominal speed of 1.1 m/s. The laser incidence angle was approximately normal to the surface of the sample in order to uniformly view the directional reflection distribution with less concern about any specular reflection components. Again, these variations between the two sets of experiments are expected to minimally affect process outcomes, particularly melt depth.

Table 4: Processing conditions unique to the directionally resolved experiments

Laser power	85 W to 485 W
Scan direction	±x
Hatch direction	-y
Gas flow speed (z = 3 mm)	1.1 m/s
Gas flow direction	-z
Laser incidence angle	(0.6 ± 0.5) °

The experimental setup for high-fidelity measurements of the directional distribution of reflected laser light is described in detail in Huang et al. [12]. The basic approach is to use a high-speed camera with a fisheye lens with a collection angle of slightly more than 180°. The dome surrounding the process is coated in a highly diffuse grey coating with reflectivity of 13.1 % at the laser wavelength of 1070 nm with a flat black base. These optical properties of the enclosure are chosen to minimize the integration of light within the enclosure to primarily image the first reflection of laser light off of the grey hemisphere. The fisheye lens is centered in the hemisphere for optimal focus on the surface and the sample is offset from the center, as illustrated in Fig. 3.

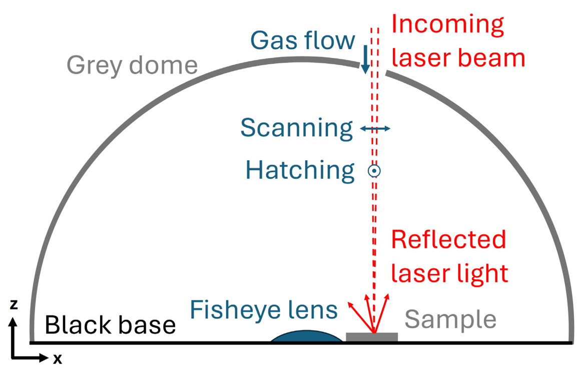

Fig. 3. Illustration of the directionally resolved experimental setup. (FIGURE WIDTH: 1 COLUMN)

Coordinate transform and image artifacts

The fisheye lens is equiangular, meaning that it generates hemispherical images on the two-dimensional imager chip through azimuthal equidistant projection. In other words, the radial distance in the image is proportional to the angle from the normal direction. Because the sample is offset from center, the images must be transformed from hemisphere-centric coordinates of the lens to sample-centric to visualize the reflected laser light distributions from the sample. Note that the distance from the center of the lens to the melt pool is approximately 31 mm, which is approximately 1/4th of the hemisphere radius, resulting in a relatively small coordinate transform. If this fraction were significantly smaller (e.g., ½), the transformation would be more significant and would reduce the accuracy at which the reflection features could be resolved.

The transformation process begins by converting each pixel from the median image into a three-dimensional vector. The horizontal and vertical positions of each pixel define its location in a coordinate system, while the pixel value itself represents the third dimension. The coordinate system is centered at the center of the dome. These vectors are then transformed from Cartesian to polar coordinates, which allows the data to be interpreted in terms of distance and angle from the center. Any vectors that fall outside the physical boundary of the measuring dome are excluded from further analysis. Next, the polar coordinates are projected onto a spherical surface to simulate the geometry of the dome. This step uses the characteristics of the fisheye lens to reverse the projection and map the data onto the hemisphere accurately. The result is a set of vectors that describe both the spatial position and the corresponding illumination value. To align the data with the actual location of the process zone, the origin of the vectors is shifted. This adjustment ensures that the reflection angles are correctly referenced to the working area. The vectors are then normalized to maintain a consistent length, representing the dome's radius. This results in a visualization of the reflection direction with the process zone acting as the origin of the rays. The effect of this coordinate transformation can be visualized Fig. 4, in which the laser inlet port translates from an off-center position to a centered position nearly normal to the sample.

The raw image data is shown on the left side of Fig. 4. The raw image data have features that are generally important and help to illustrate the effect of the coordinate transformation. First, the raw data shows "clipping," in which the smaller vertical dimension of the imager sub-window (256 pixels × 304 pixels) does not fully span the 180°, so there are no data in those small segments of the image. Secondly, the clipping and low digital levels (DL) artifacts shift and become curved, as expected. These columns of pixels exhibit signal DL that do not respond appropriately with the surrounding pixels, making lines across the image that should be disregarded.

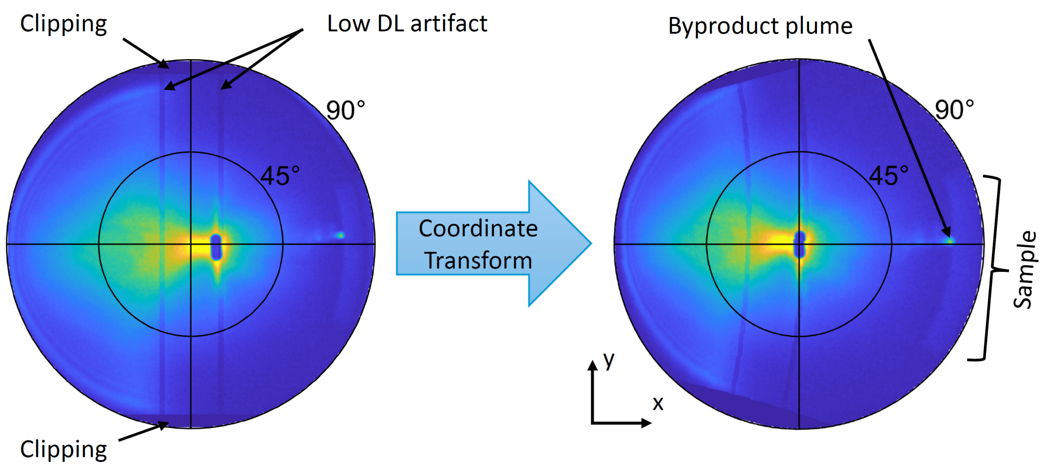

Fig. 4. Demonstration of the effect of the coordinate transform into sample coordinates from hemisphere-centric coordinates. The left image is the raw data, and the right image is the data after transformation. Laser scanning is from left to right in the positive x-direction. (FIGURE WIDTH: 1.5 COLUMNS)

An additional feature that appears in the image is that of the side of the sample near the +90° horizon. The sample is elevated such that the lens cannot directly view a first reflection of laser light from the surface of the sample, as illustrated in Fig. 3. However, laser light scattered from the plume or process byproducts can be imaged, as shown in Fig. 4. Because this light is emitted only within the beam path, omission of the data from the circle segment approximately ± 8° from the +x direction eliminates this data that should not be interpreted as reflected laser light from the melt pool.

In order to reduce the effect of the melt pool and byproducts plume thermal emission integration within the enclosure, a 1000 nm long pass filter was placed between the fisheye lens and the Si-based complementary metal oxide semiconductor (CMOS) imaging chip. Based on the transmission properties of the long pass filter and the responsivity CMOS, it is estimated that the effective wave band ranged from approximately 1000 nm to 1100 nm. Further, based on previous work [21], it is estimated that the thermal emission signal increases the apparent reflection signal by less than 3 %.

Imaging fidelity

The equiangularity of the fisheye lens transformation was tested by outfitting an equivalently sized hemisphere with equally spaced markings along the inner surface. When imaged, it was found that the spacing of the markings was within the camera pixel resolution of approximately 0.65° per pixel up to 90° off-normal in all directions.

The uniformity at which the fisheye lens collected light (or the “roll-off”) across the hemisphere was evaluated by surrounding the lens and illuminating it with a uniform hemispherical source at 850 nm [22]. It can be reasonably assumed that the roll-off is comparable at 850 nm and at the laser wavelength. It was found that the imaged signal was slightly higher in the normal direction than at the horizon. This can be systematically corrected in future work but is unnecessary for the current study. The standard deviation of the signal was less than ± 4.7 % across the 180° field of view and can be considered as a relative uncertainty in the signal.

The linearity of the camera signal response to incident power was tested by exposing the imager to a 1070 nm source, an approximately equivalent second 1070 nm source, and then both sources simultaneously. Ideally, the signal DL measured from each individual source should sum to the signal measured with both sources simultaneous. The difference ratio is a measure of the nonlinearity in the dynamic range that is covered from the individual sources to the combined sources. This is repeated throughout the dynamic range and at each integration time of interest. It was found that the most nonlinear integration time (1.25 μs) varied by as much as ± 5.8 % throughout the entire dynamic range of the camera. This can be systematically corrected for in future work; however, it is unnecessary to correct for it in the current study. These bounds in relative signal nonlinearity translate into an estimated standard relative uncertainty in signal of ± 3.3 %, per Taylor and Kuyatt [23]. Combining the components of uncertainty of the signal by root sum squares, the total relative estimated standard uncertainty in the signal is 6.5 %.

In this work, the signal level is reported in DL for a given image sequence with a fixed integration time for each image sequence. The integration time is listed with each sequence to qualitatively indicate how the reflected laser light intensity varies between image sequences. The integration times ranged from 1.25 μs to 5.0 μs. The effects of motion blur may be evaluated as future work. Similarly, the effects of laser light integration within the grey enclosure may be evaluated. The image data was taken at 60 kHz, but the results will be discussed showing every 6th frame, effectively resolving the slower dynamics of the melting process at 10 kHz. The full resolution 60 kHz data will be available in the NIST Public Data Repository [20]. The experimental methods for measuring the melt depth of the laser coupling experiments will be discussed in the following subsection.

Cross-sectioning of melt tracks

To evaluate the effect of laser power on melt depth, lengthwise cross-sections are taken along the last track of each pad scanned region, which consisted of five tracks. A multi-step process was employed to precisely cross-section tracks and verify the cross-section positions. The first step was completed with a high-speed precision saw using an alumina, rubber-bond wafering blade. This was a coarse cut, leaving about 1 mm of material remaining for removal. The samples are then held with a custom fixture and ground by hand on a grinding/polishing wheel from coarse (typically 240 grit) to fine paper (1200 grit) with intermediate steps. The custom fixture included alignment screws and a stop plate, allowing for better control of the process while facilitating for assessment using a stationary handheld microscope. Polishing was performed with a 1 μm diamond suspension followed by a 0.02 μm colloidal silica. Etching, necessary to reveal the melt track boundary, was performed by approximately 30 s submersion in Aqua Regio (3 parts hydrochloric acid to 1-part nitric acid).

Once completed, the percentage difference in melt track width was measured from top-view images taken before and after the cross-sectioning process to verify the cross-section position. The difference ranged from 46 % to 62 %, indicating that the cross-sectioning was performed through or very near the center (i.e., 50 %) of the track. The same sample preparation procedures are used for widthwise cross-sections, with the cross-section in the approximate center of each pad.

The lateral images of the longitudinal cross-sections are captured at 10× magnification using a Zeiss[1] optical microscope (Axio Imager.Z2m, Zeiss, Oberkochen, Germany). The images are processed using the Segment Anything Model (SAM) to identify and mask the melt track boundaries. SAM is an advanced image segmentation tool that uses deep learning neural networks to automatically detect and delineate objects within images, leveraging visual prompts such as points, regions of interest, or existing masks [24]. Binary masks are extracted for the melted regions from the cross-sectional images using this method, as shown in Fig. 5. The extracted masks are then exported for subsequent quantitative measurement of melt depth. In this study, "melt depth" refers to the total vertical distance from the top to the bottom of the melt track. This includes any material that may be above the initial plate surface.

Fig. 5. Example of masking out the melt track boundaries using the Segment Anything Model. The figure shows the longitudinal cross-section images of the sample with P = 285 W. (FIGURE WIDTH: 2 COLUMNS)

Computational methods

To interpret the pattern features of reflected rays recorded by the dome sensor, ray-tracing simulations have been performed using an existing multi-physics model for laser welding and additive manufacturing [25–31]. The model incorporates a numerical solver for the conservation equations of mass, momentum, and energy to simulate the thermo-fluid flow in the melt pool and the vapor plume. The level-set method is used to capture the motion of the melt pool surface, including the vapor depression wall. A ray tracing module is included to track the multiple-reflections and absorptions of the laser by the melt pool surface and vapor depression wall. Specifically, this module divides the incident beam to 64,000 rays with identical power, and the

[1] Certain equipment, instruments, software, or materials, commercial or non-commercial, are identified in this paper in order to specify the experimental procedure adequately. Such identification does not imply recommendation or endorsement of any product or service by NIST, nor does it imply that the materials or equipment identified are necessarily the best available for the purpose.

initial ray positions are sampled from a Gaussian spatial distribution to represent the beam profile. The traveling routes of and the power carried by each ray are explicitly tracked based on the formulation reported in Tan et al. [25]. Ultimately, all the rays leave the vapor depression and are intercepted by the dome in the simulations. The spatial distribution of the intercepted ray power can be drawn from the simulation results. Note that the model does not explicitly solve optical transport of reflected rays through the vapor plume. Previous modeling studies of keyhole laser welding at near-infrared wavelengths have reported that plume attenuation can be estimated using Beer's law, $\Delta I = I_0[1 - exp(-\alpha x)]$, where α is the attenuation coefficient and x is the optical path length through the plume [25]. For the present conditions, the attenuation is expected to be less than 1 % and will not significantly change the simulation results.

Results and discussion

In this section, the results of the laser coupling experiments are first translated into energy coupling per track at each power level. Then, the melt depth at the central cross-section of the pads is compared with energy coupling at each track number at four powers. These energy coupling and track depth data show the overall trends from track to track and from power level to power level. Next, the correlations between melt depth along the length of the track and dynamic coupling are established. After that, the dynamic coupling along the length of each track at several powers are described, showing the spatiotemporal behavior along the track length and from track to track. And then, the relationships between dynamic coupling, reflected laser light distributions, and melt depth are discussed to provide further insights into the physics of melting and how it may be observed through reflected laser light metrology.

Energy coupling with laser power and track number

The results of energy coupling as a function of laser power and track number are shown in Fig. 6. From 50 W to 100 W, the energy coupling increases slightly with power and does not vary significantly from track to track. As discussed in the introduction, the expected laser coupling value of roughened, solid, IN718 is approximately 0.38. The laser coupling value of less than 0.32 indicates that the laser is interacting with a nominally flat liquid surface at these low applied power levels.

From 100 W to 150 W, the energy coupling increases steeply from an average of approximately 0.33 to 0.52, indicating the formation of a vapor depression. The steepness of this increase in energy coupling with laser power appears to make the process sensitive to small perturbations, such as varying surface roughness, as evidenced by the stochasticity of the energy coupling value from track to track at each power in this range. As will be shown in the following section (Melt depth with energy coupling and track number), the widthwise cross-sections indicate that there is no overlap in melting up to 135 W, and therefore, minimal thermal exchange and heat buildup with subsequent tracks.

From 170 W to 385 W, the energy coupling continues to increase monotonically from a pad average of approximately 0.58 to 0.80. In this power range, a clear trend of increased energy coupling with increased track number emerges due to heat accumulation with increasing track number. This heat accumulation causes increasing melt pool temperatures leading to more evaporation/deeper vapor depression and correspondingly, increased energy coupling with increased melt pool depth.

From 385 W to 545 W, the energy coupling increases only subtly from a pad average of approximately 0.80 to 0.84. The trend of significantly increasing energy coupling with increasing power ceases because the energy coupling limit of the material under these processing parameters is asymptotically approached [32], taking on a value of approximately 0.85. Additionally, the trend of increasing energy coupling with increasing track number ceases due to the emergence of unstable keyholing, as evidenced by the unstable melt depth of track 5 of the 485 W pad in section after the next (Melt depth with dynamic coupling and distance along the track).

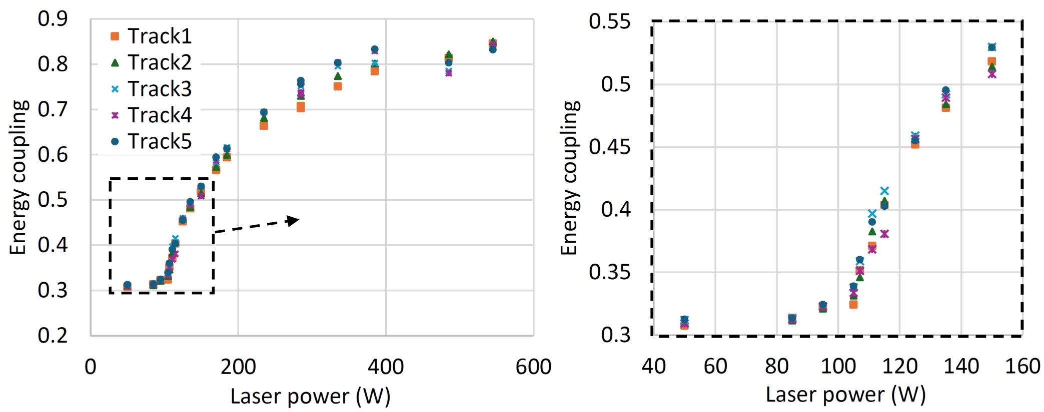

Fig. 6. Energy coupling as a function of laser power with each track of a five-track pad. The right graph is a subrange of the left graph to more closely observe the lower power results. Error bars of laser coupling uncertainty are omitted for clarity, but may be estimated from Table 3. (FIGURE WIDTH: 1.5 COLUMNS)

As discussed in the Computational methods section, a potential cause of the energy coupling limit of 0.85, or “saturation,” is laser light absorption into the byproduct plume, but this does not appear to be the case under the conditions in this work. Although the literature on each proportion of energy transfer by each mechanism is limited, previous experimental work suggests that laser light absorption into the byproduct plume is minimal in the keyholing regime (with IN625) because all of the applied laser energy (within the measurement uncertainty) can be measured with the combination of measuring reflected laser energy with the integrating hemisphere and simultaneously measuring the absorbed laser energy through calorimetry [3]. In the keyholing regime, the high velocity vapor jet is likely to rapidly eject the byproducts away from the laser beam path, resulting in minimal beam attenuation.

Therefore, the cause of the saturation appears to be primarily because liquid IN718 has a nominal energy coupling value of 0.32, corresponding to a reflectivity of approximately 0.68. The Modeling of reflected laser light distributions section discusses the reflection origins in more detail, but it can generally be expected that that some of the laser light will always be reflected from the liquid surface, especially at the front “cusp” where melting is incipient and the liquid walls are flat or only slightly angled, resulting in a single reflection of the incident light away from the melt pool that will not be absorbed into the melting process. The energy coupling limit appears to be both material and process dependent [32,3,16], but in this work energy coupling of greater than 0.80 corresponds to deep, unstable keyholing that is outside of the desirable melting regime.

Melt depth with energy coupling and track number

Cross-sections of arrays of melt tracks at four selected power levels are shown in Fig. 7. At powers of 113 W to 135 W there is no overlap from track to track and no clear trend in depth with increasing track number. At 135 W, the melt aspect ratio (2× the depth divided by the width) is approximately one, which corresponds to the upper limit of conduction mode. At 285 W there is a clear melting overlap, and the melt depth increases from track 1 to track 3 and then only subtly increases from track 3 to track 5. At 485 W the melt depth indicates deep keyholing. Additionally, there is a clear melting overlap, and the melt depth increases with each subsequent track.

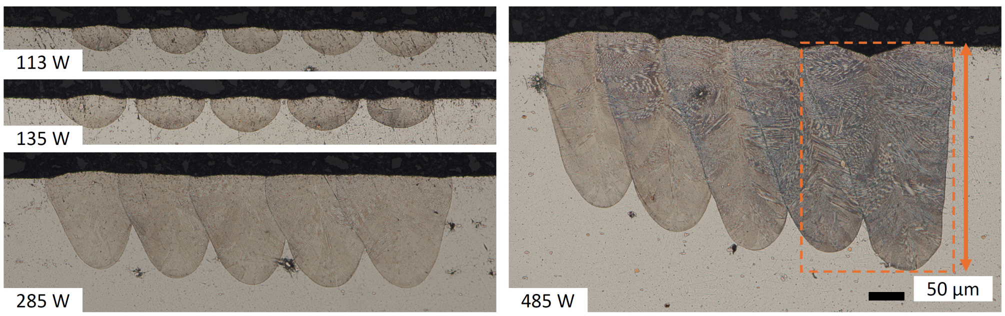

Fig. 7. Cross-sections of arrays of melt tracks at four power levels. The power level is indicated in the lower left corner of each image. The tracks are numbered 1 to 5 from left to right in the images. (FIGURE WIDTH: 1.5 COLUMNS)

The results of the centrally cross-sectioned widthwise melt depth measurements as a function of track number, energy coupling, and power are shown in Fig. 8. With powers from 113 W to 135 W, there is no clear trend in melt depth or energy coupling with increasing track number due to a lack of overlap and thermal exchange from track to track. At 285 W, the melt depth and energy coupling increase monotonically with increasing track number, except the fourth track shows slightly lower energy coupling than would be expected. The general increase in energy coupling with melt depth from track to track suggests that the two measurands may be correlated under these conditions.

At 485 W, the energy coupling remains approximately constant at a value near 0.8 while the melt depth increases with track number due to heat accumulation in the pad. The lack of increase in energy coupling with track number, coexisting with increasing melt depth with track number, indicates a decorrelation between energy coupling and melt depth at this high power. The correlation and decorrelation between melt depth along the length of a track and dynamic coupling are further discussed in the following section.

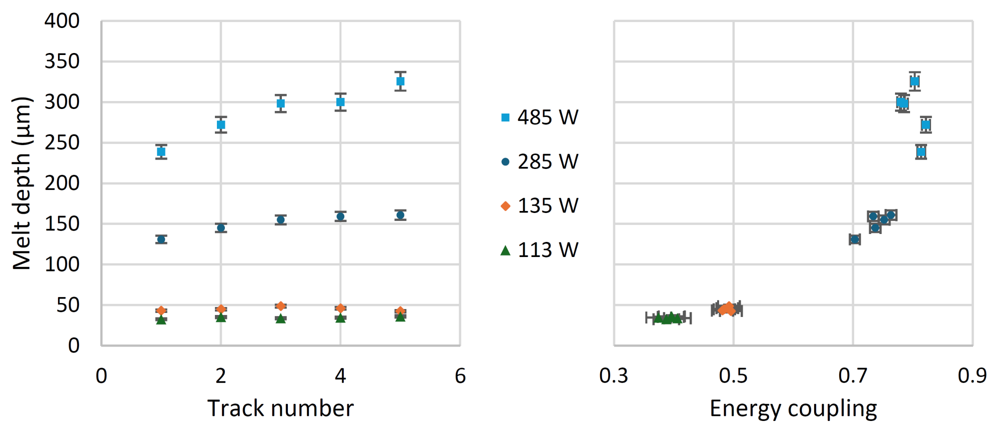

Fig. 8. Melt depth as a function of track number and energy coupling, at the selected laser powers. The vertical axes on both graphs are the same, as are the symbols for power. The error bars represent the estimated standard relative uncertainty (Type B, k = 1) in melt depth per Weaver et al. [15], and the uncertainty in energy coupling is listed in Table 3. (FIGURE WIDTH: 1.5 COLUMNS)

Melt depth with dynamic coupling and distance along the track

Images of sample cross-sections of the track 5 melt boundary are shown in Fig. 9. The results showed that the melt track depth increased with higher laser power. The deepest melt tracks are observed at the highest power setting of 485 W, while the shallowest melt tracks occurred at the lowest power of 113 W. Additionally, there was a consistent spike in melt track depth at the start of each track, although the length over which this occurred varied among the samples. Note that the light spots within the 485 W melt track are simply inconsistencies in the etch appearance and not keyhole defects.

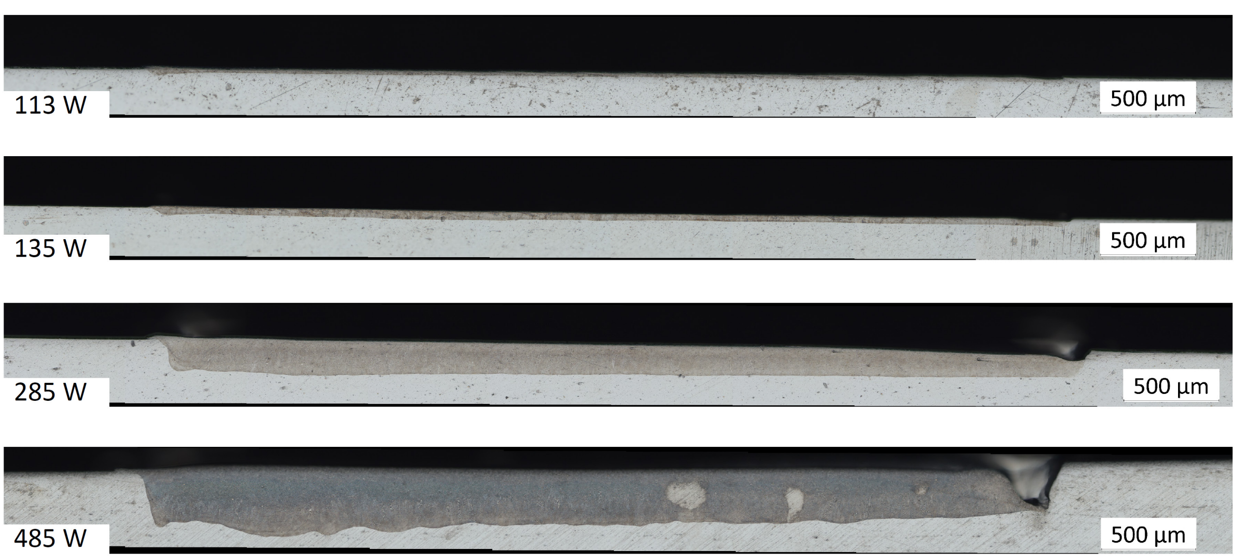

Fig. 9. Lengthwise cross-sections of samples at different laser power levels. (FIGURE WIDTH: 2 COLUMNS)

The melt depth and dynamic laser coupling with distance along track 5 of each pad are shown in Fig. 10. The data are plotted on both the left and right axes with limits set at ± 30 % of the mean value of the corresponding measurand. The final 1 mm of data is removed to eliminate the erroneous apparent depth due to the solidified vapor depression at the termination of each track. The melt depth data are spatially aligned with the dynamic coupling data by the first data point that exceeded 30 % of the mean value of each measurand. This approach is estimated to have a standard uncertainty (Type B, k = 1) within one-half the laser beam radius at ± 18 μm.

With powers of 113 W and 135 W, the initiation of the track (first 500 μm) shows a significant spike in both depth and dynamic coupling. This initial spike is related to the vapor depression shape, and this will be further discussed in the section after the next (Track formation and reflected laser light). With powers of 113 W, 135 W, and 285 W, the melt depth and dynamic coupling are strongly correlated with correlation coefficients of $\rho > 0.5$, which indicates that the instantaneous melt depth can be predicted from the dynamic coupling value under these melting conditions. At 485 W, the melt depth and dynamic coupling become negligibly correlated with $\rho < 0.2$, which corresponds to the material and process saturation limit of 0.80 in this work. Although the instantaneous melt depth cannot be predicted from the dynamic coupling value under this condition, exceeding a dynamic coupling saturation limit indicates unstable keyholing that is outside of the desirable melting regime.

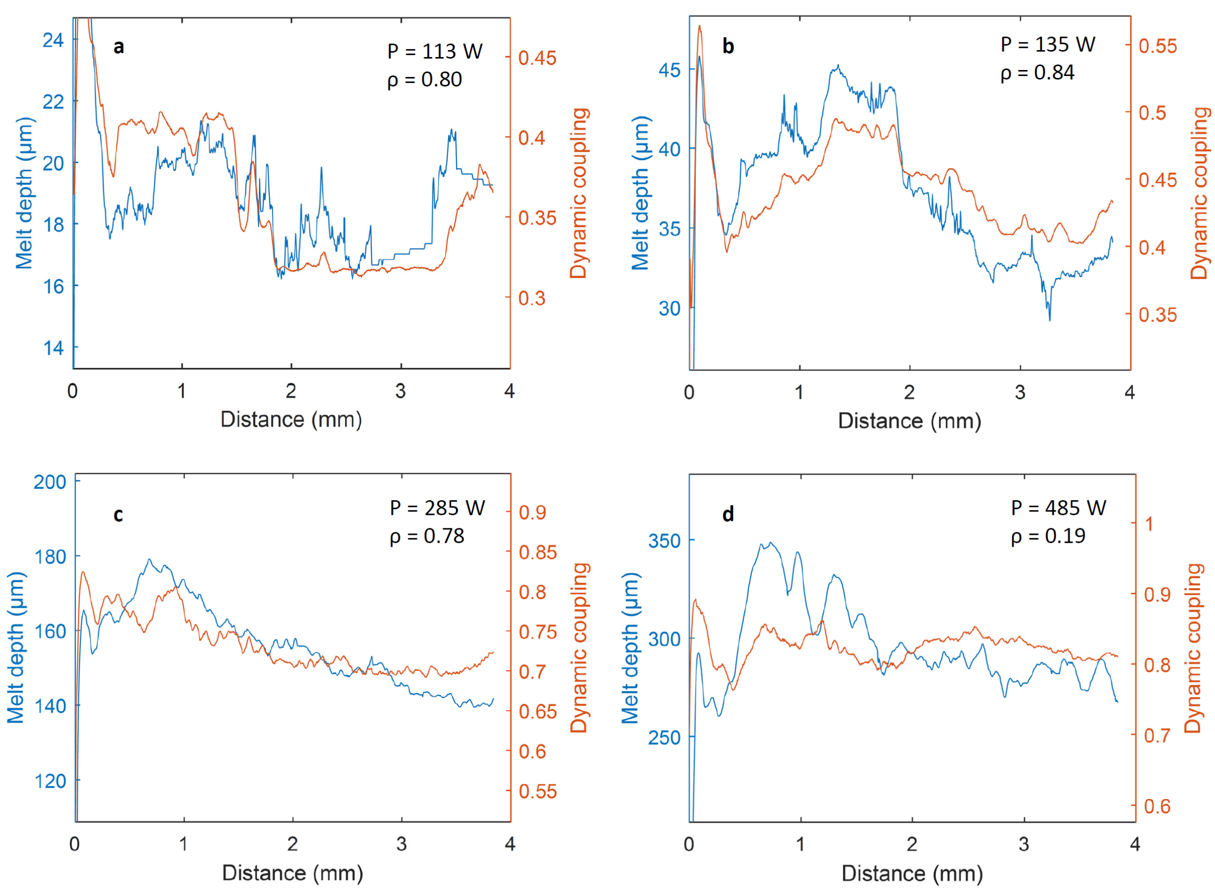

Fig. 10. Melt depth and dynamic laser coupling with distance along the fifth (last) track of a pad at four power levels (P) with associated correlation coefficients (ρ). A distance of 0 mm indicates the beginning of the track and the last 1 mm of the track was removed. (FIGURE WIDTH: 2 COLUMNS)

Dynamic coupling with laser power and track number

The results of dynamic laser coupling measurements with track distance and track number at six laser powers are shown in Fig. 11. At a power of 85 W (Fig. 11a), and after the first 0.5 mm, each track develops an approximately equivalent and constant value of approximately 0.32 along the track length with some relatively small and infrequent spikes along the way. As discussed previously, this indicates a stable melting process and a relatively flat and smooth molten surface.

At powers of both 113 W and 135 W (Fig. 11b-c), the dynamic coupling jumps to about 150 % of the nominal value within the first 0.5 mm of the track. After track formation, the dynamic coupling varies stochastically about its nominal value along the length of the track, with no clear trend from track to track (noting that the nominal coupling value is increased from 113 W to 135 W).

At 185 W (Fig. 11d), within the first 0.5 mm, the dynamic coupling value of each track exhibits an initial jump to approximately 125 % of that of the end of the track. At this power and in the distance range of 0.5 mm to 2 mm, a trend emerges that the dynamic coupling value increases with each subsequent track, indicating that heat accumulation occurs primarily toward the beginning of the track. Knowing that laser coupling is correlated with melt depth, this indicates deeper melting at the initiation of each subsequent track due to the end of each previous track being hotter than the last (likely molten with a scan turnaround time of only 0.75 ms) at this laser power level.

At 285 W (Fig. 11e), each track exhibits an initial peak in the first 0.5 mm. Then, from 0.5 mm to the end of the track, a clear trend emerges with the dynamic coupling consistently increasing with each subsequent track. This, again, indicates that heat accumulation occurs primarily at the beginning of each track, but also continues for the entire length of the track at 285 W.

Finally, at 485 W (Fig. 11f), each track exhibits an initial peak and valley within the first 1 mm of track length and then maintains a relatively constant value for the remainder of the track. The dynamic coupling tends to increase with track number. But track 3 appears to be an outlier, which further corroborates the weak correlation between laser coupling and melt depth at this high-power deep keyholing mode. The relations between track formation, melt depth, laser coupling, and reflected laser light distributions will be described in the following section.

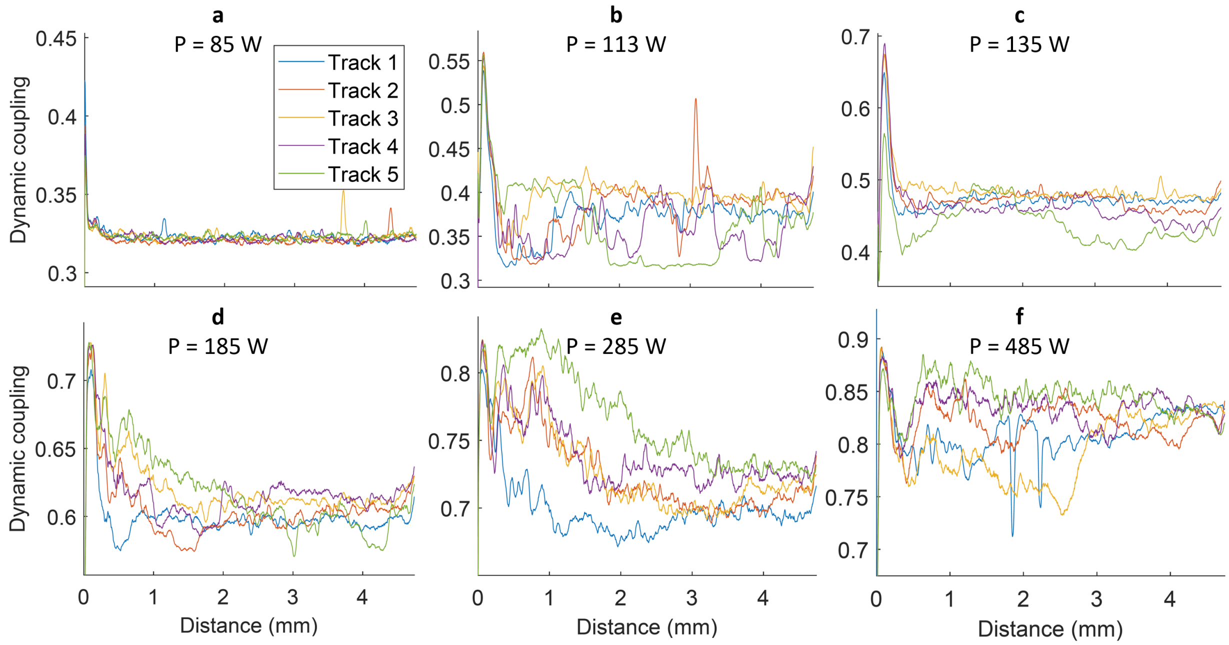

Fig. 11. Dynamic laser coupling with track distance and track number at six laser powers. Note that distance along the track is from its initiation point, whether or not it is scanned in +y or -y. (FIGURE WIDTH: 2 COLUMNS)

Track formation and reflected laser light

This section describes the results of melt depth, dynamic coupling, and reflected laser light distributions in the first 0.4 mm of track formation of track 5 of the previous sections (Melt depth with dynamic coupling and distance along the track and Dynamic coupling with laser power and track number). Under the melting conditions of this study, it is found that all tracks approach a steady-state melt pool by a distance of 0.4 mm from track initiation. This section will focus on the dynamics of track formation within this distance range, with future work to focus more closely on steady-state reflected light signals.

As described previously, lengthwise cross-sections are only taken for powers of 113 W, 135 W, 285 W, and 485 W. The camera was not synchronized with the laser turn-on, therefore, it is assumed that one-half the laser scan distance between frames is the nominal location of the first frame that images a laser reflection. This results in the first frame being assigned a location of 0.008 mm along the length of the track. The imager integration time is indicated on the left of each image sequence and dynamic coupling pair shown in the figures in this section.

Conduction mode

At a power of 85 W (Fig. 12a), at a distance of 0.008 mm along the track, a hazy reflection distribution appears. At the same location, the dynamic coupling jumps to a maximum value of approximately 0.38, as described in the Introduction section. Additionally, the reflected laser distribution exhibits a near-normal glossy reflection at a relatively small solid angle as would be expected when reflecting off a roughened solid metallic surface. And so, both the dynamic coupling and the reflected light distribution both show clear evidence of the short moment before the phase transition to liquid.

At a power of 85 W (Fig. 12a) and at 0.104 mm, a concentric ring pattern emerges in the directional reflection distribution, and the distribution extends toward the front of the melt pool more than the rear. This reflection distribution indicates a primarily specular reflection from a shallow and smooth melt pool depression. Concentric ring patterns are evidently related to constructive and destructive interference. These interference patterns may potentially be used to extract information about the vapor depression shape in future work. At this distance, the dynamic coupling value is approximately 0.33, indicating the beginning of multiple reflections within the shallow vapor depression. From 0.200 mm to 0.392 mm, the reflected light distribution shifts toward the rear of the melt pool and the concentric ring pattern remains, indicating that the front wall of the vapor depression has become steeper than the rear wall as the well-known teardrop shape develops. A C-shaped pattern of bright reflection also forms. In this range, the dynamic coupling remains approximately constant.

Increasing the power to 113 W (Fig. 12b), the trends in distributions of reflected light are comparable, but with a couple of differences. The first difference is that the distributions cover a significantly larger solid angle at each distance compared to 85 W, which indicates that the walls of the vapor depression have become steeper. Secondly, the bright areas take on a more complex pattern at a distance 0.200 mm beyond, with two streaks pointing toward the rear of the melt pool, as well as lobes forming on either side. Similarly to the 85 W track, the dynamic coupling of the 113 W track reaches a value of approximately 0.38 at a distance of 0.008 mm before the transition to liquid occurs. The dynamic coupling value then dips slightly at 0.020 mm as the transition to liquid occurs, but before a vapor depression can form.

At the power of 113 W (Fig. 12b) and in the distance range of 0.075 mm to 0.104 mm, the dynamic coupling value and the melt depth peak. Similarly, at 0.104 mm, the largest solid angle of the reflected light occurs, which also corresponds to the peak in dynamic coupling and melt depth as the vapor depression walls steepen and facilitate more internal reflections within the depression [12]. Beyond 0.104 mm, solid angle of reflection decreases and shifts toward the rear of the melt pool as the initially circular depression transitions into a teardrop shape that facilitates fewer reflections within the depression.

At 135 W (Fig. 12c), a new feature emerges at 0.104 mm in which almost the entirety of the hemisphere is illuminated with the highest signal intensity at approximately 50 % of the peak value in the plotted range, and the first appearance of radial streaks. This pattern again corresponds to the peak in dynamic coupling and melt depth. Beyond the 0.104 mm, the trends described in the 113 W track continue, with an increase in solid angle of the reflected light distribution at each distance, along with the streak and lobe features becoming more defined.

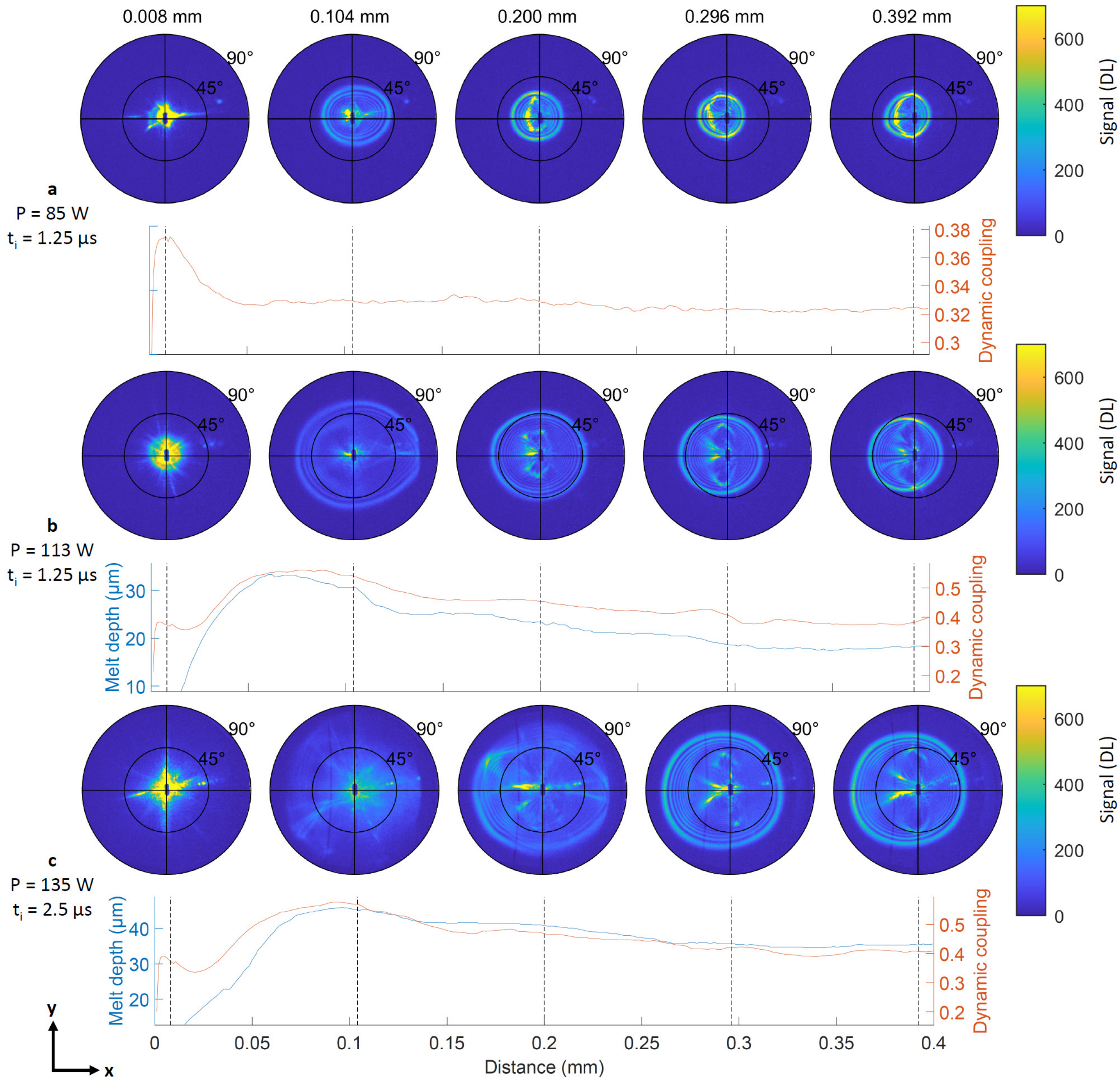

Fig. 12. Melt depth, dynamic coupling, and reflected laser light distributions in the first 0.4 mm of track formation at three powers (P): a) 85 W, b) 113 W, and c) 135 W. The imager integration time is indicated by t_i. There was no lengthwise cross-section depth measurement for (a). (FIGURE WIDTH: 2 COLUMNS)

Keyhole mode

As discussed in the results of the "Melt depth with energy coupling and track number" section, the power of 135 W may be considered the end of conduction mode because the melt track aspect ratio (2× the depth divided by the width) has reached a value of one. In keyhole mode, multiple reflections in the vapor depression are dominant, resulting in an overall shift in the distributions of reflected laser light.

At 185 W and at 0.008 mm (Fig. 13a), the solid angle of the hazy reflection distribution is significantly increased compared with the conduction mode tests. This significantly larger solid angle suggests that the laser is interacting with a surface that has been previously melted, or is still molten, in addition to the adjacent ground wrought surface. This is further evidenced by the initial plateau in the dynamic coupling value at 0.008 mm is significantly greater than the expected ground solid surface value of 0.38 that appears at this location in conduction mode at all three of the higher powers. In contrast, at 0.104 mm, the reflected laser light distribution appears qualitatively similar to the same distance with a laser power of 135 W with the majority of the hemisphere illuminated, minimal spikes in intensity, and radial streak patterns.

Conversely, from 0.200 mm to 0.392 mm at 185 W, the reflected light distributions bare minimal resemblance to the distributions that developed at lower powers in the same lengths along the track. In this range, radial streak patterns remain in the distribution, with patterns concentrated at approximately 135° and 225° azimuthally from the front of the melt pool (+x). Additionally, a peak in intensity emerges near 0° from normal (+z). Moreover, another intense feature in the image appears near the +x horizon at approximately 80° from normal, emanating from the surface of the sample and existing within the laser beam path. This indicates the formation of a nominally hemispherical vapor depression during the transition to a deeper keyhole. The origin of the characteristics of the reflection distribution as steady state melting is approached (0.392 mm and beyond) will be further elucidated in the Modeling of reflected laser light distributions section.

At powers of 285 W (Fig. 13b) and 485 W (Fig. 13c), the reflected laser distributions exhibit similar features to those of the first portion of the 185 W track, a large solid angle hazy reflection distribution forms at 0.008 mm and then evolves into a more uniformly illuminated hemisphere with minimal peaks in intensity at 0.104 mm. Additionally, at hazy reflection distribution continues to correspond to a plateau in the dynamic coupling at 0.008 mm, with the plateau value increasing slightly with each increase in power. Furthermore, the location of 0.104 mm corresponds to a peak in dynamic coupling. From 0.200 mm to 0.392 mm at 285 W, the reflected light distributions continue to resemble those of the 185 W track but are increasingly dynamic, and the area of high intensity near-normal (+z) has increased. These trends continue with power increased to 485 W in the range of 0.200 mm to 0.392 with the distributions becoming rather chaotic with a large and dynamic high intensity area oscillating about 0°.

The column of light emanating from the surface at the sample near the forward horizon is generated by reflected laser light, and potentially thermal emission, from the plume of process byproducts (e.g., spatter or condensate) and their interaction with the incoming laser beam. The size and intensity of the light generated by byproducts increases with distance along the track and with power.

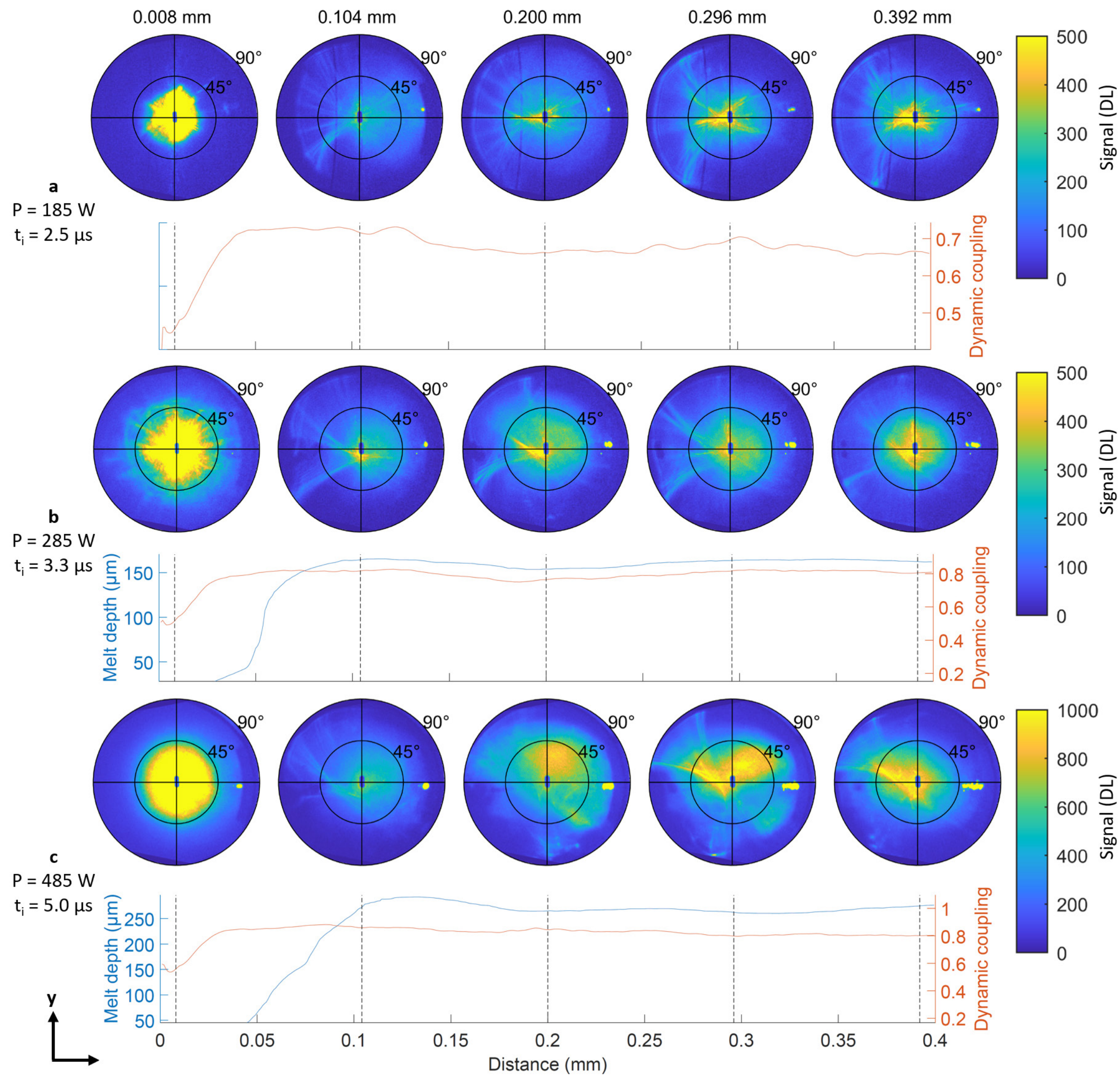

Fig. 13. Melt depth, dynamic coupling, and reflected laser light distributions in the first 0.4 mm of track formation at three powers (P): a) 185 W, b) 285 W, and c) 485 W. The imager integration time is indicated by t_i. There was no lengthwise cross-section depth measurement for (a). (FIGURE WIDTH: 2 COLUMNS)

Modeling of reflected laser light distributions

Comparing experimental measurements with modeling results helps to evaluate the fidelity of either approach. Whether evaluated experimentally or computationally, the reflection distributions observed in this work are controlled by the local slopes and curvature of the vapor depression surface. And so, favorable agreement between the measurement and simulation results indicate that the main vapor-depression geometry is represented. Simulation results are compared with experimental measurements for three laser powers: 185 W, 285 W, and 485 W at scanning speed of 960 mm/s. The 185 W case is close to the transition from a shallow vapor depression toward keyholing, while the 285 W and 485 W cases represent keyhole conditions with different melt-pool and vapor depression depths. These cases are selected to test the model across different melting conditions at nominally steady conditions (at a distance beyond the dynamics of track formation), as well as to investigate the origins of the prominent streaking features under these conditions.

Before evaluating the reflected light distributions, the simulated melt-pool depths are compared with the experimental Track 1 melt-track depths reported in Fig. 8. Track 1 was used for this comparison because the simulations represent a single-track process and do not include consideration for heat accumulation from adjacent tracks. The simulated melt-pool depths are approximated 160 μm at 285 W and 259 μm at 485 W, which are consistent with the corresponding experimental depths of approximately 130 μm and 240 μm, respectively. This agreement indicates that the simulations provide a reasonable prediction of the melt-pool dimensions before the reflected ray distributions are analyzed.

The reflected light distribution predicted by the ray-tracing simulation is then compared with experimentally measured reflection distribution, as shown in Fig. 14. For the 285 W case, the simulated and experimental distributions in Fig. 14a and Fig. 14b qualitatively resemble each other, with prominent radial streaks extending radially and slightly toward the rear of the melt-pool. To make the comparison more quantitative, the hemisphere was divided into 12 sectors, and the reflected intensity in each sector was integrated; the ray intensity from both simulation and experiment are first summed in each sector then normalized by the total value across the whole hemisphere to normalize the intensity before comparison. As shown in Fig. 14c-e, all three cases show favorable agreement in the dominant high-intensity sectors and the overall distribution across all sectors. This agreement supports the reliability of the model in predicting the predominant features of the reflection distributions.

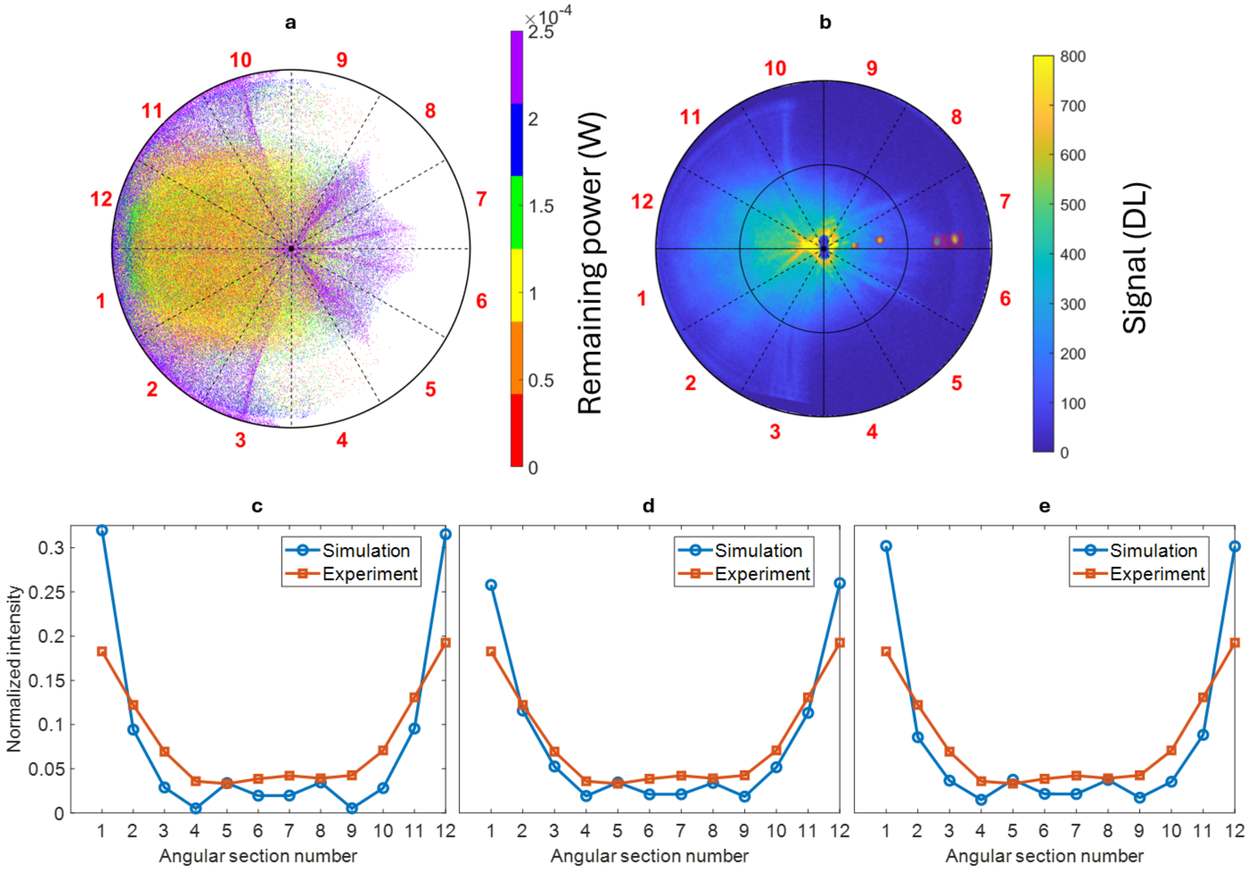

Fig. 14. Comparison between simulated and experimental reflection distributions: a) ray tracing simulation of the hemispherical reflection distribution at 285 W; each marker represents the interception location of a ray and the colors denote the remaining ray power, b) experimental measurement under the same conditions as (a), c) normalized ray intensity comparison for 185 W, d) normalized ray intensity comparison for 285 W, e) normalized ray intensity comparison for 485 W (FIGURE WIDTH: 2 COLUMNS)

The detailed ray-origin analysis in the following focuses on the 285 W case because it shows clear streak features and good agreement between the simulated and experimental reflection distributions. To produce less congested distribution maps, only half of the beam intensity profile is considered by splitting the incident beam, as shown in Fig. 15a, and the incident beam is subdivided into eight spatial regions. Fig. 15b shows the original locations of all the incident rays, with the colors denoting the number of reflections of each ray during its entire interaction with the vapor depression. Abundant rays near the front and side edges of the laser spot (in Regions I, V, VI, VII, and VIII) are colored dark blue, indicating only one reflection for their traveling routes. In contrast, rays with their original locations closer to the center and the tail of the laser profile (primarily in Regions II, III, and IV) exhibit more reflection counts on their routes. For the rays originating (reflecting) from each of the eight regions, the locations of their final interception by the dome are plotted in Fig. 15c, with the colors denoting the number of reflections experienced by each ray. It is interesting to find that all the rays responsible for the streak pattern on the dome are those from Regions I, V, VI, VII, and VIII with only one reflection in their entire traveling routes. Other rays experienced multiple reflections, and the distributions of those rays on the dome are diffuse and primarily toward the rear of the melt pool.

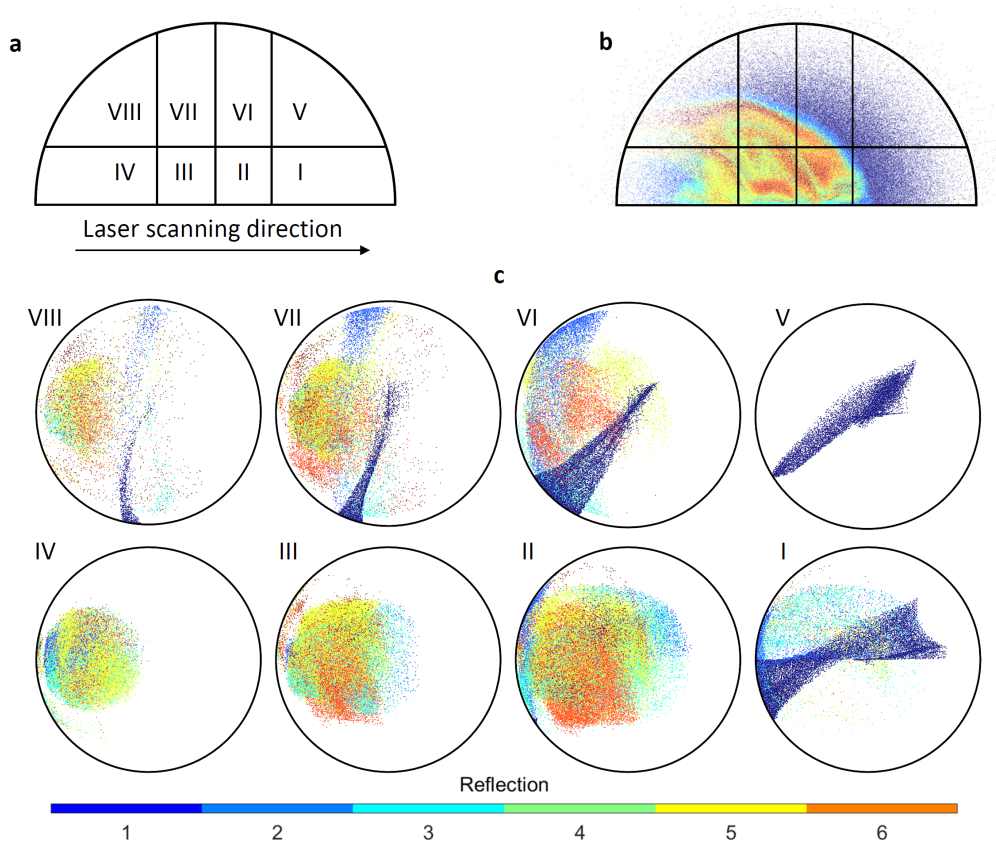

Fig. 15. Analysis of origins of all reflected rays: a) shows the division of the incident rays into eight spatial regions, b) shows the spatial distribution of all rays based on their original incidence location, with the color denoting the total reflection count of each ray, c) shows the hemispherical distribution of all reflected rays each region defined in (a). (FIGURE WIDTH: 1.5 COLUMNS)

Fig. 16 presents the locations of all ray reflections over the entire vapor depression. The streak features on the dome are found to be associated with the regions near the front and side edges of the laser profile with only one reflection. These rays illuminate the top surface of the substrate in front of the vapor depression as well as the edge of the vapor depression, as labeled in Fig. 16a. Their reflection directions are generally upward, so the rays will depart the substrate without any additional reflections.

The curvature of the vapor depression entrance (labeled by the dashed curve) helps to converge all the reflected rays into a slender region on the dome (i.e., the streak), and the direction of the streak on the dome should be generally perpendicular to the tangent direction of the curve. At the melt pool cusp (Regions I and V in Fig. 16b and Fig. 16c), a rippled wave is produced above the substrate surface and rays impinging on this region form the radial streaks in front of the melt pool.

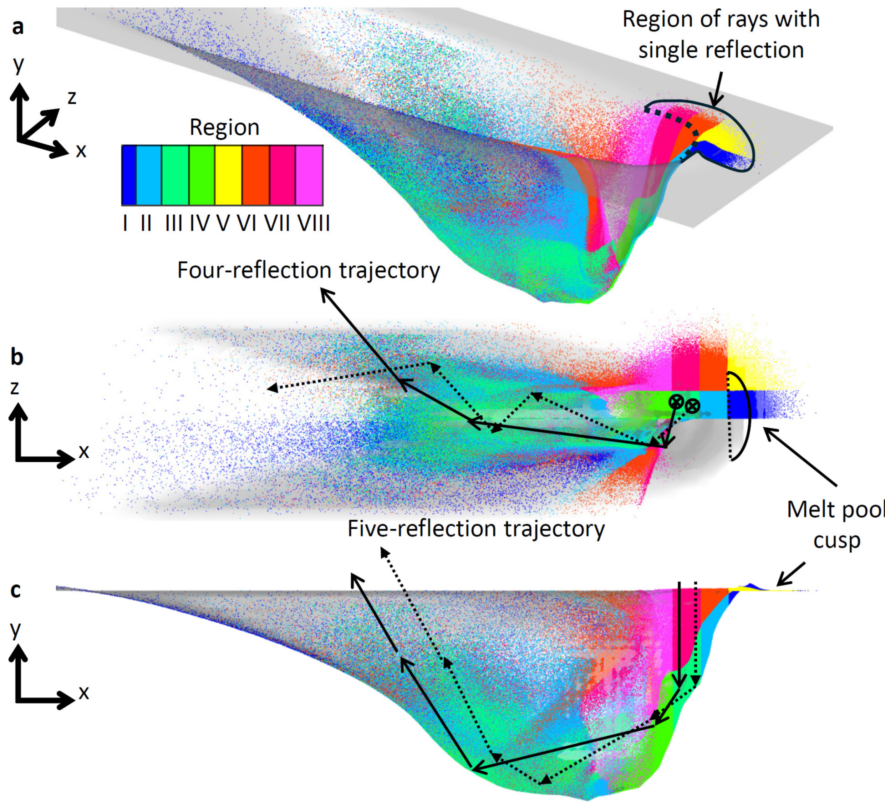

Fig. 16. Locations of multiple reflections for all rays on the vapor depression wall from: a) isometric, b) top, and c) side views. Each reflection point is colored by the initial location of the ray. (FIGURE WIDTH: 1.5 COLUMNS)

Fig. 16 shows that the other rays enter the vapor depression and experience multiple reflections, with the reflection counts varying between four to six (shown in Fig. 15b). The variation of reflection count is attributed to the local differences of the vapor depression wall slope. The traveling routes of two example rays are highlighted in Fig. 16b and Fig. 16c. While the two rays enter the vapor depression at similar locations, the marginal differences in the local vapor depression wall slopes for their first reflections lead the two rays traveling along slightly different directions. One ray ultimately generates one more reflection on the vapor depression wall than the other ray.

Two aspects merit comment regarding practical translation of this research. First, the present system combines directionally resolved reflection imaging, an integrating hemisphere, and ray-tracing simulation to provide the resolution needed for diagnosing melting physics and validating multi-physics models [13], not for in-situ deployment; the optical access requirements of the domes conflict with the build-chamber, recoating, and gas-flow constraints of production PBF-LB/M machines. Second, the bare-plate substrates used here permitted these relationships to be isolated cleanly, whereas an actual powder bed, being rougher and more heterogeneous, would broaden and randomize the reflection signature through multiple scattering [28] and introduce layer-to-layer effects (residual porosity, partially melted particles, spatter, denudation) [30] that further alter absorption and reflection, compounding the surface-roughness sensitivity already observed here between 100 W and 150 W. Neither point diminishes the present results; rather, they indicate the path to application. The physical relationships established here, particularly between melting mode, vapor depression formation, laser coupling, and the directional reflection signature, provide the basis for designing and interpreting simplified, sensors into manufacturing machines, such as one described in [11], that operate with reduced resolution and angular coverage under real powder-bed conditions. Advancing such reduced-complexity systems to application readiness, informed by the present high-fidelity findings and validated melt pool models, is the focus of ongoing work.

Conclusions

This paper provides a glimpse into the abundance of information that can be detected with reflected laser light measurements in processing of nickel superalloy 718. Dynamic coupling and melt depth along the track are strongly correlated when the power levels are slightly above the vapor depression threshold, within the unstable conduction mode melting regimes, and up until the material and process coupling limit is approached. This indicates that the instantaneous melt depth can be predicted as long as the dynamic coupling value remains less than 0.80 in this combination of material and processing conditions.

The dynamics of track formation can be observed by measuring the reflected laser light. A hazy reflection distribution occurs when the incoming laser interacts with a solid metal surface; the dynamic coupling also takes on a constant value of approximately 0.38 with IN718. A broader solid angle of reflection corresponds to higher dynamic coupling and deeper melt depth both along the length of a track at constant power, as well as with increased laser power levels within conduction mode. The transition from conduction mode is clearly indicated by a shift in the character of the reflection distribution from a steady and nominally circular pattern with concentric rings to having radial streaks. High-fidelity computational modeling with ray tracing shows that the streaks originate from a single reflection from surface ripples at the cusp of the melt pool.

Analysis of the reflected light measurements have been limited to those during melt track formation and to selected steady-state model validation cases in this work. However, further insights can undoubtedly be gained with additional data analysis and modeling of the process physics, and the data used in this publication are to be published through the NIST Public Data Repository. Translating the present diagnostics and capabilities into practical process monitoring in operational manufacturing machines will require simplified, retrofittable hardware adapted to real powder bed conditions.

Contributions

David Deisenroth: Conceptualization; Data curation; Formal analysis; Investigation; Methodology; Resources; Software; Supervision; Validation; Visualization; Writing – original draft; Writing – review and editing. **Jordan Weaver**: Conceptualization; Formal analysis; Investigation; Methodology; Resources; Supervision; Validation; Writing – review and editing. **Nismath Valiyakath Vadakkan Habeeb**: Conceptualization; Formal analysis; Investigation; Software; Writing – original draft; Writing – review and editing. **Kevin Chou**: Project administration; Resources; Supervision; Writing – review and editing. **Moritz Wittemer**: Conceptualization; Formal analysis; Investigation;

Methodology; Software; Validation; Visualization; Writing – review and editing. **Katrin Wudy**: Project administration; Resources; Supervision; Writing – review and editing. **Haoran Shi**: Conceptualization; Formal analysis; Investigation; Software; Writing – original draft; Writing – review and editing. **Wenda Tan**: Project administration; Resources; Supervision; Writing – review and editing.

Declaration of competing interests

The authors declare that they have no known competing financial interests or personal relationships that could have appeared to influence the work reported in this paper.

Acknowledgements

The NIST researchers in this work were funded by the United States Government. Work conducted by the University of Louisville team was partially supported by the National Science Foundation (CMMI-1921263), under INTERN supplemental funding. Work conducted by the University of Michigan team was partially supported by the National Science Foundation (CMMI-2119671).

References

[1] D. Swift-Hook, A. Gick, Penetration welding with lasers, Weld. J. 52 (1973) 492s–499s.
[2] Remy Fabbro, Dionisio Bermejo, Jose M. Orza, Lilian Sabatier, Laurent Leprince, Vincent Granier, Absorption measurements in continuous high-power CO2 laser processing of materials, in: 1990: pp. 461–467. https://doi.org/10.1117/12.20566.
[3] David C. Deisenroth, Sergey Mekhontsev, Brandon Lane, Measurement of mass loss, absorbed energy, and time-resolved reflected power for laser powder bed fusion, in: 2020. https://doi.org/10.1117/12.2547491.
[4] G. Teodorescu, Radiative emissivity of metals and oxidized metals at high temperature, (2007).
[5] T.H. Kim, C.E. Albright, S. Chiang, The Energy Transfer Efficiency in Laser Welding Process, J. Laser Appl. 2 (1990) 23–28. https://doi.org/10.2351/1.4745249.
[6] J. Trapp, A.M. Rubenchik, G. Guss, M.J. Matthews, In situ absorptivity measurements of metallic powders during laser powder-bed fusion additive manufacturing, Appl. Mater. Today 9 (2017) 341–349.
[7] M. Wittemer, K. Wudy, Intensity-dependent absorption signature for in situ process characterization in laser processing of 316L, Int. J. Adv. Manuf. Technol. 133 (2024) 3497–3512. https://doi.org/10.1007/s00170-024-14008-6.
[8] B. Lane, I. Zhirnov, S. Mekhontsev, S. Grantham, R. Ricker, S. Rauniyar, K. Chou, Transient Laser Energy Absorption, Co-axial Melt Pool Monitoring, and Relationship to Melt Pool Morphology, Addit. Manuf. 36 (2020) 101504. https://doi.org/10.1016/j.addma.2020.101504.
[9] S.A. Khairallah, T. Sun, B.J. Simonds, Onset of periodic oscillations as a precursor of a transition to pore-generating turbulence in laser melting, Addit. Manuf. Lett. 1 (2021) 100002. https://doi.org/10.1016/j.addlet.2021.100002.
[10] B.A. Mehmetli, K. Takahashi, S. Sato, Direct measurement of reflectance from aluminum alloys during CO2 laser welding, Appl. Opt. 35 (1996) 3237–3242. https://doi.org/10.1364/AO.35.003237.
[11] M. Wittemer, F. Ferle, K. Wudy, In-line process monitoring in laser welding and powder bed fusion of metals using directional reflection measurements, J. Laser Appl. 36 (2024) 042025. https://doi.org/10.2351/7.0001559.

[12] W. Huang, D. Deisenroth, S. Mekhontsev, W. Tan, Correlation between keyhole geometry and reflected laser light distribution in laser-based manufacturing, Manuf. Lett. 38 (2023) 56–59. https://doi.org/10.1016/j.mfglet.2023.09.002.
[13] L. Levine, B. Lane, E. Glaessgen, M. Gorelik, Providing a Rigorous Benchmark Measurement Foundation for Modeling-Informed Qualification and Certification of Metal Additive Manufactured Components, JOM 76 (2024) 1897–1904. https://doi.org/10.1007/s11837-024-06388-7.
[14] E.H. Glaessgen, M. Gorelik, C.C. Battaile, D. Lamm, L.E. Levine, H.R. Millwater, A. Peralta-Duran, N. Raghavan, A.D. Rollett, E.J. Schwalbach, Computational Materials for Qualification and Certification (CM4QC) Strategy Document: Maturation of Computational Materials Methods for Aviation-Focused Qualification and Certification of Metal Additive Manufacturing (as an Example of Process-Intensive Materials), National Aeronautics and Space Administration, 2026.
[15] J.S. Weaver, D. Deisenroth, S. Mekhontsev, B.M. Lane, L.E. Levine, H. Yeung, Cross-Sectional Melt Pool Geometry of Laser Scanned Tracks and Pads on Nickel Alloy 718 for the 2022 Additive Manufacturing Benchmark Challenges, Integrating Mater. Manuf. Innov. 13 (2024) 363–379. https://doi.org/10.1007/s40192-024-00355-5.
[16] G. Nordet, C. Gorny, Y. Mayi, J. Daligault, M. Dal, A. Effernelli, E. Blanchet, F. Coste, P. Peyre, Absorptivity measurements during laser powder bed fusion of pure copper with a 1 kW cw green laser, Opt. Laser Technol. 147 (2022) 107612. https://doi.org/10.1016/j.optlastec.2021.107612.
[17] P.Y. Shcheglov, A.V. Gumenyuk, I.B. Gornushkin, M. Rethmeier, V.N. Petrovskiy, Vapor–plasma plume investigation during high-power fiber laser welding, Laser Phys. 23 (2012) 016001.
[18] D Deisenroth; S Mekhontsev; S Grantham, Design and Calibration of the Fundamentals of Laser-Matter Interaction (FLaMI) Powder Bed Fusion Testbed at the National Institute of Standards and Technology, NIST Adv. Manuf. Ser. AMS 100–66 (n.d.). https://doi.org/https://doi.org/10.6028/NIST.AMS.100-66.
[19] J. Weaver, D. Deisenroth, S. Mekhontsev, J. Redford, B. Lane, AMB2025-06 and AMB2025-07 Challenge Problem Calibration Data, (n.d.). https://doi.org/https://doi.org/10.18434/mds2-3707.
[20] National Institute of Standards and Technology, Science Data Portal, (n.d.).
[21] David Deisenroth, Sergey Mekhontsev, Brandon Lane, Leonard Hanssen, Ivan Zhirnov, Vladimir Khromchenko, Steven Grantham, Daniel Cardenas-Garcia, Alkan Donmez, Measurement Uncertainty of Surface Temperature Distributions for Laser Powder Bed Fusion Processes, J. Res. NIST 126 (2021). https://doi.org/10.6028/jres.126.013.
[22] David C. Deisenroth, Leonard Hanssen, Sergey Mekhontsev, High temperature reflectometer for spatially resolved spectral directional emissivity of laser powder bed fusion processes, in: 2020. https://doi.org/10.1117/12.2568179.
[23] B.N. Taylor, C.E. Kuyatt, Guidelines for evaluating and expressing the uncertainty of NIST measurement results, National Institute of Standards and Technology, 1994.
[24] A. Kirillov, E. Mintun, N. Ravi, H. Mao, C. Rolland, L. Gustafson, T. Xiao, S. Whitehead, A.C. Berg, W.-Y. Lo, Segment anything, in: 2023: pp. 4015–4026.
[25] W. Tan, N.S. Bailey, Y.C. Shin, Investigation of keyhole plume and molten pool based on a three-dimensional dynamic model with sharp interface formulation, J. Phys. Appl. Phys. 46 (2013) 055501. https://doi.org/10.1088/0022-3727/46/5/055501.
[26] W. Tan, Y.C. Shin, Analysis of multi-phase interaction and its effects on keyhole dynamics with a multi-physics numerical model, J. Phys. Appl. Phys. 47 (2014) 345501. https://doi.org/10.1088/0022-3727/47/34/345501.

[27] N. Kouraytem, X. Li, R. Cunningham, C. Zhao, N. Parab, T. Sun, A.D. Rollett, A.D. Spear, W. Tan, Effect of Laser-Matter Interaction on Molten Pool Flow and Keyhole Dynamics, Phys. Rev. Appl. 11 (2019) 064054. https://doi.org/10.1103/PhysRevApplied.11.064054.
[28] X. Li, C. Zhao, T. Sun, W. Tan, Revealing transient powder-gas interaction in laser powder bed fusion process through multi-physics modeling and high-speed synchrotron x-ray imaging, Addit. Manuf. 35 (2020) 101362. https://doi.org/10.1016/j.addma.2020.101362.
[29] X. Li, Q. Guo, L. Chen, W. Tan, Quantitative investigation of gas flow, powder-gas interaction, and powder behavior under different ambient pressure levels in laser powder bed fusion, Int. J. Mach. Tools Manuf. 170 (2021) 103797. https://doi.org/10.1016/j.ijmachtools.2021.103797.
[30] F. Li, I. Bitharas, A.J. Moore, W. Tan, Effects of gas composition and pressure level on powder spattering and denudation in laser powder bed fusion, Acta Mater. 299 (2025) 121443. https://doi.org/10.1016/j.actamat.2025.121443.
[31] F. Li, H. Shi, N. Kirschbaum, C. He, C.E. Okwudire, W. Tan, Elucidating the mechanism for suppression of spatter in dual-laser powder bed fusion systems: A numerical and experimental study, Addit. Manuf. 118 (2026) 105102. https://doi.org/10.1016/j.addma.2026.105102.
[32] J. Ye, S.A. Khairallah, A.M. Rubenchik, M.F. Crumb, G. Guss, J. Belak, M.J. Matthews, Energy Coupling Mechanisms and Scaling Behavior Associated with Laser Powder Bed Fusion Additive Manufacturing, Adv. Eng. Mater. (2019) 1900185.